Enhancing the Efficiency and Stability of Tin-Lead Perovskite Solar Cells via Sodium Hydroxide Dedoping of PEDOT:PSS

*Dong-Tai Wu ‡[a], Wen Xian Zhu ‡[a], Yueyao Dong[b], Matyas Daboczi[c], Gayoung Ham[d], Hsing-Jung Hsieh[a], Chi-Jing Huang[a], Weidong Xu[f], Charlie Henderson[e], Ji-Seon Kim[e], Salvador Eslava[c], Hyojung Cha[d,f], Thomas J. Macdonald [b], Chieh-Ting Lin [a,h]**

a. Department of Chemical Engineering, National Chung Hsing University, 145 Xingda Road, Taichung 402-27, Taiwan

b. School of Engineering and Materials Science, Queen Mary University of London, London E1 4NS, UK

c. Department of Chemical Engineering and Centre for Processable Electronics, Imperial College London, SW7 2AZ, London, UK

d. Department of Energy Convergence and Climate Change, Kyungpook National University, Daegu 41566, Republic of Korea

e. Department of Physics and Centre for Processable Electronics, Imperial College London, London SW7 2AZ, UK

f. Department of Hydrogen and Renewable Energy, Kyungpook National University, Daegu 41566, Republic of Korea

g. Department of Chemical Engineering and Biotechnology, University of Cambridge, Philippa Fawcett Drive, Cambridge, CB3 0AS UK

h. Innovation and Development Center of Sustainable Agriculture, National Chung Hsing University, Taichung City, 402, Taiwan

* Corresponding author. Email: c.lin15@nchu.edu.tw

‡ *These authors contributed equally to this work.*

Keywords: Sn-Pb perovskite, PEDOT:PSS, doping, charge carrier recombination, narrow-bandgap perovskite

Abstract

Tin-lead (Sn-Pb) perovskite solar cells (PSCs) have gained interest as candidates for the bottom cell of all-perovskite tandem solar cells due to their broad absorption of the solar spectrum. A notable challenge arises from the prevalent use of the hole transport layer, PEDOT:PSS, known for its inherently high doping level. This high doping level can lead to interfacial recombination, imposing a significant limitation on efficiency. Herein, we use NaOH to dedope PEDOT:PSS, with the aim of enhancing the efficiency of Sn-Pb PSCs. Secondary ion mass spectrometer profiles indicate that sodium ions diffuse into the perovskite layer, improving its crystallinity and enlarging its grains. Comprehensive evaluations, including photoluminescence and nanosecond transient absorption spectroscopy, confirm that dedoping significantly reduces interfacial recombination, resulting in an open-circuit voltage as high as 0.90 V. Additionally, dedoping PEDOT:PSS leads to increased shunt resistance and high fill factor up to 0.81. As a result of these improvements, the power conversion efficiency is enhanced from 19.7% to 22.6%. Utilizing NaOH to dedope PEDOT:PSS also transitions its nature from acidic to basic, enhancing stability and exhibiting less than a 7% power conversion efficiency loss after 1176 h of storage in N_2 atmosphere.

Introduction

The power conversion efficiency (PCE) of perovskite solar cells (PSCs) has been a focus of intense research in recent years.[1,2] Single junction Pb-only PSCs have achieved remarkable PCEs exceeding 26%, [3,4] due to the efforts on interface engineering,[5–8] composition optimization,[9–11] defect passivation,[12–14] post-treatment[15–17] and charge transport layer development.[18–21] Specifically, formamidinium lead iodide ($FAPbI_3$), with a bandgap of around 1.48 eV, has achieved the highest PCE to date for lead-only materials, a value of 26.1 %. [3,4] While single-junction Pb-only PSCs are approaching their theoretical efficiency limits, increasing attention is being directed towards Sn-Pb PSCs due to their bandgap's proximity to the optimal value dictated by the Shockley-Queisser limit for single-junction solar cells.[22] The structural similarity between Sn and Pb allows for easy substitution of Sn into the ABX_3 perovskite lattice without compromising its structure. Interestingly, by altering the Sn-to-Pb ratio, the bandgap of these mixed perovskites can be fine-tuned in a range of approximately 1.25 to 1.4 eV, which is below the bandgap of both Sn-only or Pb-only perovskites.[23] The noticeable nonlinearity in the bandgap of Sn-Pb hybrid perovskite alloys is primarily due to chemical variables, particularly due to mismatched energy levels between the *s* and *p* atomic orbitals of Pb and Sn that delineate the alloy's band edges.[24] This emphasizes the potential of Sn-Pb perovskite in achieving the

highest PCE among single junction solar cells by optimizing the bandgap to be close to 1.35 eV.[22] Additionally, by further reducing the bandgap of mixed Sn-Pb PSCs to around 1.25 eV, these cells can serve as the bottom layer in an all-perovskite tandem device configuration when combined with a wide-bandgap perovskite top cell.[25–28] This arrangement facilitates absorption across a broad spectrum of sunlight, including the near-infrared region, thus elevating the efficiency beyond the confines of the Shockley-Queisser limit. Efficiencies beyond 23.7% have been recorded for single-junction Sn-Pb PSCs,[29,30] while all-perovskite tandem structures have achieved record PCEs of up to 29.1%. [31]

Nowadays, efficient Sn-Pb PSCs are predominantly fabricated in a p-i-n inverted structure.[23] However, the efficiency of hybrid Sn-Pb PSCs still lags behind Pb PSCs, partially due to a significant open-circuit voltage (V_{OC}) deficit relative to the energy bandgap (E_g). Minimizing the oxidation of Sn^{2+} to Sn^{4+} [32–34] and passivating the defects, including intrinsic point defects[35] (such as Sn and Pb vacancies and antisites) and extrinsic defects[36–38] (such as impurities and grain boundaries), are efficient approaches for reducing the V_{OC} loss originating from the Sn-Pb perovskite layer. [28,39–43] Another key consideration pertains to the interface between the perovskite and the charge transport layer. The selection of both hole transport layers (HTL) and electron transport layers (ETL), particularly the control of energy band alignment, can have a profound impact on the V_{OC}.[44] Considering the conduction band minimum of Sn-Pb perovskite is shaped by the *p* orbitals of both lead (Pb) and iodine (I), prevalent ETLs such as C60 and PCBM, which excel in Pb-only perovskites, have been adapted for Sn-Pb perovskites, yielding notable device performance. Furthermore, the utilization of fullerene derivatives, such as IPH and IPB, with a shallower LUMO level than C60, has led to similar V_{OC} enhancements in both Pb-only[45] and Sn-Pb perovskites [46] systems. This underscores the versatility of these ETLs, demonstrating their effectiveness in both Pb-only PSCs and Sn-Pb PSCs.

On the other hand, choosing an appropriate HTL poses a greater challenge. It demands consideration of not only the bandgap alignment but also the compatibility with the growth of Sn-Pb perovskite on the HTL surface. Since the valence band maximum of Sn-Pb perovskite results from the interaction between the *s* orbital of Sn and the *p* orbital of iodine, Sn-Pb perovskites may obtain a shallower valence band compared to Pb-only perovskites. As such, HTLs that have proven stable and efficient in Pb-only PSCs, such as polymer semiconductors, poly[bis(4-phenyl)(2,4,6-trimethylphenyl)amine (PTAA), and NiOx, have not yielded satisfactory efficiency in Sn-Pb PSCs. Up to now, only a limited number of research groups have successfully developed efficient Sn-Pb PSCs using alternative HTLs like hole selective monolayers

[47] and ternary tin (II) alloys.[48] In contrast, PEDOT: PSS still remains the most commonly used HTL in Sn-Pb PSCs, with a recorded PCE of 23.6%.[40] Consequently, there has been a significant effort to optimize PEDOT:PSS for Sn-Pb PSCs, including surface modifications using hydroquinone and polyethylene glycol,[49,50] as well as reducing the thickness of PEDOT:PSS.[49]

Interestingly, while PEDOT:PSS has been highlighted as a potential HTL choice for Sn-Pb PSCs, PEDOT:PSS has also been associated with significant V_{OC} loss in Pb-only PSCs.[51,52] The V_{OC} loss with PEDOT:PSS is due to its highly doped nature resulting from the PSS stabilization of positive charges (polarons or bipolarons) on the PEDOT chains, maintaining PEDOT in the continuously doped state. In the doped condition, a substantial population of resident holes is available for recombination with electrons from the conduction band of the lead-based perovskite, resulting in interfacial recombination that contributes to the reduction of the V_{OC}.[52,53] Reducing the doping level of PEDOT:PSS can effectively decrease recombination and increase V_{OC} in Pb-only PSCs.[53] In a recent work by Chin et al., NaOH was employed to dedope PEDOT:PSS effectively suppressing the interfacial recombination in a methylammonium lead iodide ($MAPbI_3$) device, resulting in a notable 90 mV increase in V_{OC}.[53] These findings underscore the substantial impact of controlling the doping level of HTLs on minimizing interfacial recombination and enhancing device performance. Nevertheless, the excessive doping in PEDOT:PSS does not cause V_{OC} loss in organic solar cells[54] and remains unknown if it does in Sn-Pb PSCs. Pb-only and Sn-Pb PSCs often show different behavior, and Sn-Pb perovskites with less-doped HTLs like PTAA have not shown higher V_{OC} compared to those with PEDOT:PSS.[40,46,55]

In this study, we demonstrate that although PEDOT:PSS is commonly used as an HTL in Sn-Pb perovskite devices, its highly doped nature can lead to surface recombination as it does in Pb-only PSCs, limiting their V_{OC}. To dedope the PEDOT-PSS HTL and study its doping effects on Sn-Pb PSCs, NaOH is herein researched as a multi-functional additive serving to enhance both their V_{OC} and stability. We show that NaOH effectively deprotonates the acidic sulfonated groups in PEDOT:PSS, reducing the hole population in the material, which leads to a 300 meV shallower Fermi level. Moreover, upon growing the Sn-Pb perovskite layer on the dedoped PEDOT:PSS and annealing, secondary ion mass spectrometry (SIMS) reveals that sodium ions from the dedoped PEDOT:PSS diffuse into the Sn-Pb perovskite layer improving crystallinity and enlarging grain its grains. Photoluminescence (PL) and nanosecond transient absorption spectroscopy (ns-TAS) results in dedoped PEDOT:PSS/Sn-Pb-perovskite films show that the dedoping of PEDOT:PSS significantly reduces interfacial

recombination, indicated by enhanced PL signal and longer lifetime. Dedoping PEDOT:PSS also reduces its dark carrier density and thus improves the selectivity for efficient hole transport. This enhancement boosts the shunt resistance of the devices, which results in a significant enhancement of the fill factor (FF) leading to a remarkable overall increase of PCE from 19.7% to 22.6% for Sn-Pb PSCs. Utilizing dedoped PEDOT:PSS also results in improved storage stability, exhibiting only 7% loss in PCE compared to a 37% PCE loss of the reference after 1176 hours. Our study provides substantial guidance for the development of highly efficient single-junction Sn-Pb PSCs and offer significant implications for the progress of all-perovskite tandem solar cells.

Results and Discussion

NaOH was applied to adjust the doping level of PEDOT:PSS. NaOH regulates both the carrier concentration and the pH of the HTL.[53,56] **Figure 1a** illustrates the dedoping mechanism of PEDOT:PSS by NaOH.[53] The hydroxide ions react with the sulfonate groups in PSS, resulting in deprotonation. This process effectively neutralizes the acidity of PSS and facilitates the formation of PSS-Na. Since the sulfonate groups play an important role in the stabilization of polarons an bipolarons of PEDOT the transformation to PSS-Na leads to a reduction in charge carrier density.[57] The dedoping of PEDOT:PSS with NaOH can be probed with measurements of work function and conductivity.[57–59] For a fair comparison, the thicknesses of pristine and dedoped films are maintained the same (at ~30 nm) by controlling the spin-coating speed. The work function and conductivity were measured by Kelvin probe (KP) and transfer length method (TLM).

Figure 1b demonstrates the changes in the work function of the PEDOT:PSS film with different NaOH volume ratios. Initially, the work function of the unmodified PEDOT:PSS film is 4.59 eV. However, it decreases to 4.52 eV with 5 vol% NaOH and further down to 4.32 eV with 10 vol% NaOH. Interestingly, when the NaOH is further increased to 20 vol%, there is a rebound in the work function, up to 4.46 eV, but still below the starting 4.59 eV. The significantly decreased work function values suggest that NaOH reduces the hole concentration, effectively dedoping the PEDOT:PSS.

As the charge carrier density of PEDOT:PSS is reduced by dedoping, the conductivity of these films is also expected to decrease by the addition of NaOH. **Figure 1c** shows the conductivity of the pristine and dedoped PEDOT:PSS films. The conductivity of pristine PEDOT:PSS thin film is 2800 μS/cm, whereas after dedoping the conductivity showed a significant decrease to 1300 μS/cm (10 vol% NaOH) and 700 μS/cm (20 vol% NaOH). Nonetheless, it was observed that PEDOT:PSS with 5

vol% NaOH demonstrated an increased conductivity of approximately 4200 µS/cm. This aligns well with previous studies and implies an increased ionic contribution to the conductivity due to the increased concentration of sodium ions brought into the system by the NaOH solution [53].

Atomic force microscopy (AFM) is further employed to investigate the surface morphological changes of these films (**Figure 1d**). The root-mean-square roughness (R_q) decreased from 4.45 nm for pristine PEDOT: PSS to 3.45 nm and 1.72 nm for the films dedoped with 5 vol% and 10 vol%, respectively. However, with a further increase in NaOH to 20 vol%, an obvious aggregation is observed, with the R_q increasing to 8.98 nm. The substantial increase in surface roughness likely contributes to surface inhomogeneities, potent enough to cause local fluctuations in the work function. This can cause variations in both abnormal trends of conductivity and work function of PEDOT:PSS at this higher NaOH ratio.[59–62]

Interestingly, the film treated with 5 vol% NaOH displays slightly higher conductivity but a lower work function compared to the pristine PEDOT:PSS films. This increased conductivity suggests that at low doping the ionic current from Na+, combined with a small change in surface morphology, outweighs the effect of reduced hole density. Conversely, the film treated with 20 vol% NaOH exhibits a rise in the work function but a decrease in conductivity compared to its 10 vol% NaOH counterpart. This could be attributed to the over fivefold R_q increase measured by AFM, highlighting that both charge carrier density and morphology impact the conductivity of PEDOT:PSS. [59]

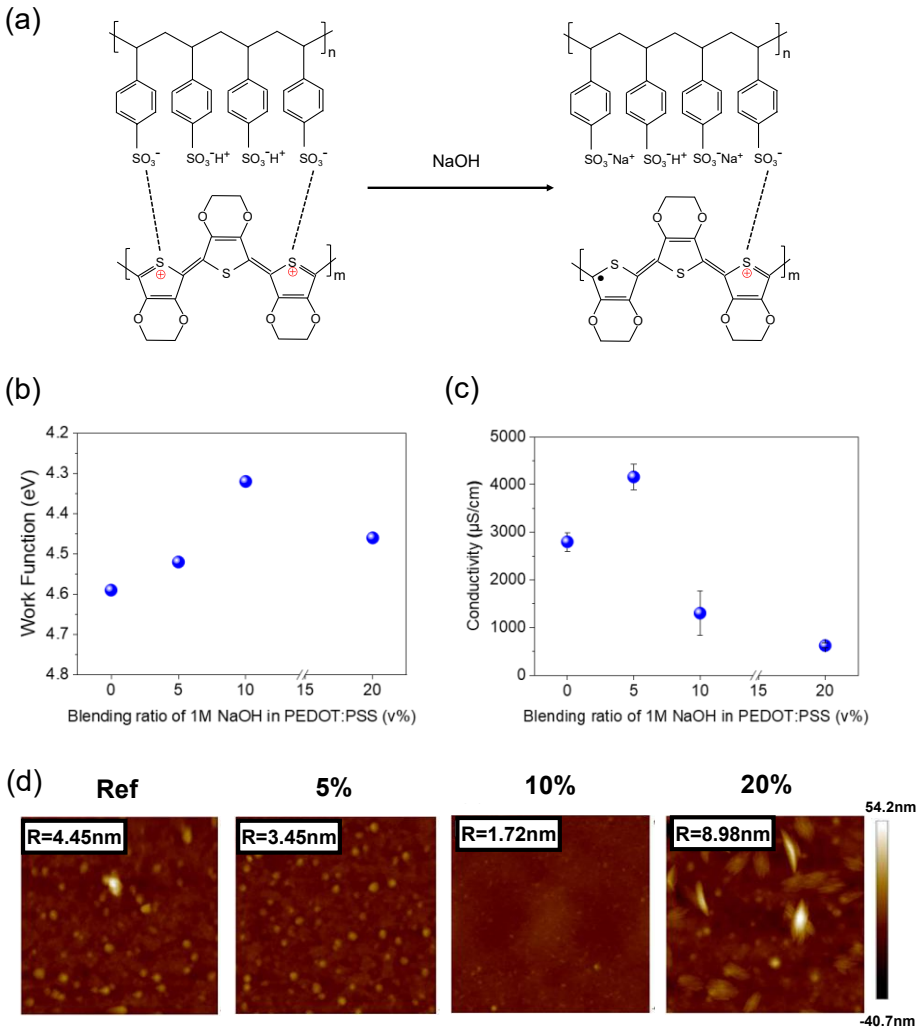

Figure 1. (a) Schematic mechanism of PEDOT:PSS dedoping by NaOH. (b) Conductivity, (c) work function, and (d) AFM topographic images for pristine PEDOT:PSS and dedoped with 5, 10, and 20 vol% volume ratio of NaOH solution.

We then turn the consideration to the Sn-Pb perovskite layer grown on the pristine and dedoped PEDOT:PSS. A one-step anti-solvent method was used to deposit a low bandgap mixed Sn-Pb perovskite, $Cs_{0.025}FA_{0.475}MA_{0.5}Sn_{0.5}Pb_{0.5}I_{2.925}Br_{0.075}$. The visible absorption spectrum and Tauc plot of the perovskite film are shown in **Figure S1**, indicating that the bandgap of Sn-Pb perovskite is ~1.29 eV. Drawing a lesson from the study of Pb-only perovskites, previous reports have demonstrated that sodium ions can enhance crystallinity and facilitate grain size enlargement.[63,64] Therefore, it is crucial to investigate whether sodium ions in PEDOT:PSS can play a similar role in Sn-Pb perovskites.

Secondary ion mass spectrometry (SIMS) with 10 keV Ar cluster ion beam with positive polarity was used to characterize the elemental depth profiles of perovskite grown on the dedoped PEDOT:PSS, as shown in **Figure 2a** for the 10 vol%. NaOH sample**.** The profiles of O^+, Sn^+ and Pb^+ ions were employed to discern the perovskite/PEDOT:PSS interface. A pronounced increase in O^+ intensity originating from the PEDOT:PSS layer, coupled with a simultaneous decrease in Sn^+ and Pb^+ ions within the perovskite layer, serves as a distinct indicator of a well-defined perovskite/PEDOT:PSS interface. Remarkably, in contrast to the O^+ profile, Na^+ ions are not exclusively confined to the PEDOT:PSS layer; instead, they are dispersed throughout the entire perovskite film, with higher intensity at the perovskite film's surface and the interface between perovskite and PEDOT:PSS. This provides evidence for sodium ions readily penetrating the perovskite layer during the crystallization process.

We further employed X-ray diffraction (XRD) to evaluate the crystallinity of the perovskite on these PEDOT:PSS substrates. As illustrated in **Figure 2b**, on the dedoped PEDOT:PSS substrate, the intensity of the (110) diffraction peak is enhanced compared to the one on pristine PEDOT:PSS, with the highest intensity for the 10 vol% NaOH sample. The Scherrer equation was used to estimate the crystallite size by analyzing the full width at half maximum (FWHM) of the diffraction peak **(**Figure 2c).[65,66] The crystallite size increases from 42.4 to 47.4 nm for the perovskite grown on PEDOT:PSS with 10 vol% NaOH. This suggests a potentially better-ordered crystalline structure of the perovskite on the dedoped substrate.

Scanning electron microscopy (SEM) was utilized to investigate the surface morphologies of perovskite on dedoped PEDOT:PSS substrates. As illustrated in **Figure 2e-g**, the surface morphology reveals notable morphology differences and grain sizes in the grown perovskites on the different PEDOT:PSS layers. The average grain size increases from 572 to 718, 781, and 892 nm with 0, 5, 10, and 20 vol% NaOH used, respectively. Therefore, the existence of PSS-Na is beneficial in improving the quality

of the Sn-Pb perovskite by enlarging the grains and reducing the number of grain boundaries.[63,64] However, visible pinholes appeared between grains for the 20 vol% samples, which could be detrimental to the device performance. As such, the optimal concentration appears to be 10 vol% NaOH in terms of enhanced perovskite crystallinity and grain size.

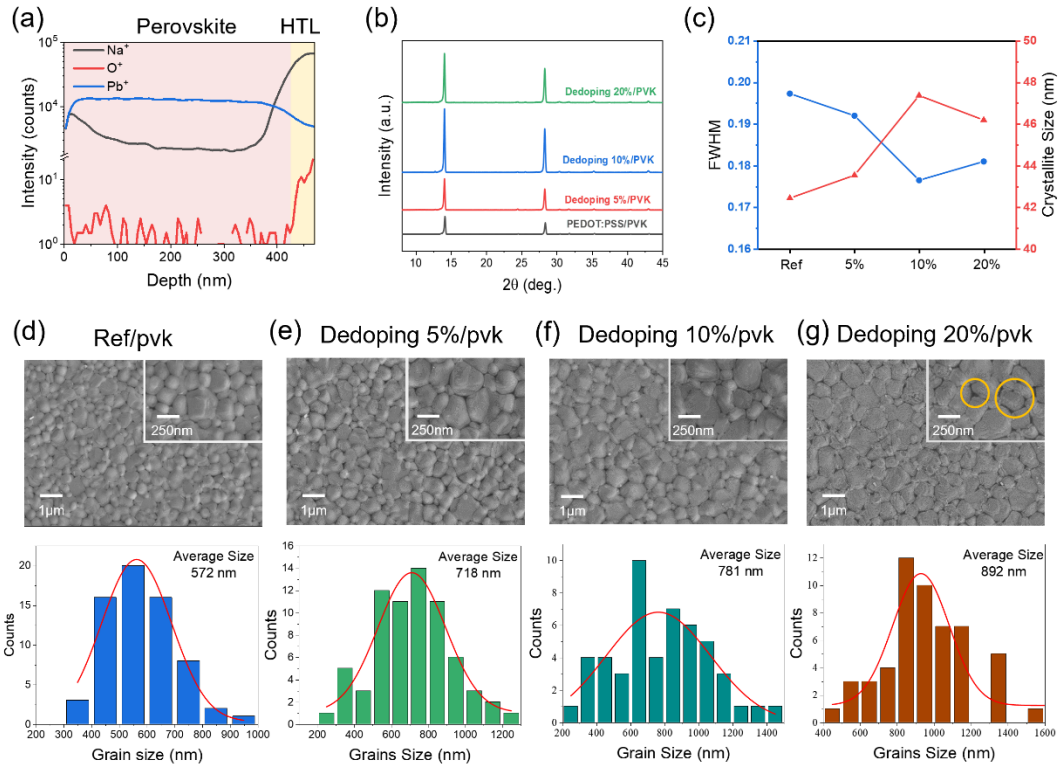

Figure 2. (a) Time-of-flight secondary ion mass spectrometry (ToF-SIMS) depth profile of Sn-Pb perovskite film grown on PEDOT:PSS dedoped by 10 vol% NaOH.(b) The XRD patterns of perovskites grown on dedoped PEDOT:PSS. (c) Full width at half maximum (FWHM) values, accompanied by the corresponding crystallite sizes for each sample. (d) SEM micrographs and associated grain size distribution of Sn-Pb perovskite, referred to as 'pvk' in labelling, grown on pristine PEDOT:PSS, as well as on PEDOT:PSS dedoped by various volume ratio of NaOH: (e) 5%, (f) 10%, (g) 20%.

Furthermore, it has been shown that utilizing a hydrophobic HTL can effectively enhance the separation between perovskite nuclei, leading to larger grain sizes and enhanced crystalline quality.[66] To determine if the change in perovskite grain size and crystallinity is linked to variation in the contact property between the perovskite precursor and PEDOT:PSS layer, contact angle measurements were conducted on the dedoped PEDOT:PSS layers, as depicted in **Figure S2**. The measurements revealed contact angles ranging from 10 to 13 degrees, a range that is within the experimental error margin. Consequently, it can be deduced that the variations in contact angle are

not the predominant factor influencing the observed increase in grain size and improved crystallinity herein. All the characterization together demonstrates that sodium ions diffuse into the Sn-Pb perovskites enhancing its crystallinity and promoting grain size enlargement, in agreement with previous reports.[63,64]

To comprehend the influence of dedoping PEDOT:PSS on device performance, PSCs were fabricated with an ITO/HTL/Sn-Pb perovskite/C60/BCP/Ag structure. Here, the HTL represents PEDOT:PSS prepared with varying volume ratios of NaOH solution. Photovoltaic parameter statistics are presented in **Figure 3a-f** and summarized in **Table 1**. The average PCE increases from 19.1% (±0.6) for pristine PEDOT:PSS to 19.8% (±0.5) and 21.3% (±0.8) with 5 and 10 vol% NaOH application, respectively. However, a further increase in NaOH to 20 vol% leads to a decreased PCE of 18.6% (±1.2). A closer examination reveals that the observed PCE enhancement for moderate NaOH application is strongly correlated with improvements in both V_{OC} and FF. Specifically, average V_{OC} values increase systematically from 0.85 (±0.01) on pristine PEDOT:PSS to 0.86 (±0.01) and 0.88 (±0.01) V with 5 and 10 vol% NaOH, respectively. Similarly, average FF values exhibit a positive shift from 74.1% on pristine PEDOT:PSS to 75.5% and 79.1% with 5 and 10 vol% NaOH application, respectively, coinciding with an increase in shunt resistance R_{sh}, as shown in Figure 3f. In the case of extensive dedoping with 20 vol% NaOH in PEDOT:PSS, all parameters experience a notable decline. This is primarily attributed to the aggregation of PEDOT:PSS, as depicted in **Figure 1d**, and the emergence of pinholes within the perovskite layer, as shown in **Figure 2d**. These adverse factors collectively contribute to a significant decrease in all key performance parameters under this high dedoping condition.

This study highlights 10 vol% NaOH as the optimal blend ratio. **Figure 3g** illustrates the J-V characteristics of champion devices using both pristine PEDOT:PSS and PEDOT:PSS dedoped with 10 vol% NaOH. The champion device employing pristine PEDOT:PSS as HTL reports a PCE of 19.7%, V_{OC} of 0.85 V, J_{SC} of 31.6 mA/cm², and FF of 73.5%. In contrast, the champion device with dedoped PEDOT:PSS achieves a PCE of 22.6%, V_{OC} of 0.89 V, J_{SC} of 31.6 mA/cm², and FF of 80.2%. This condition also achieved a V_{OC} of 0.90 V with a slightly lower J_{SC}. Details of reverse and forward scans for these devices can be found in **Figure S3** and **Table S1**, respectively. The external quantum efficiency (EQE) for these devices is depicted in **Figure S4a-b**. The band gaps measured through EQE for the device using reference and dedoped PEDOT:PSS are 1.28eV and 1.29eV, respectively. These values closely align with those determined by the visible absorption spectrum. The dark current (**Figure 3h**) in the shunt region (below 0.2 V) of the dedoped sample reveals a decrease compared to the reference, indicating reduced current leakage. This observation agrees well with

increased FF and R_{sh} (**Figure 3e-f**). Generally, PEDOT:PSS, has a high density of dark carriers (both electrons and holes) and it is electrically conductive for both carrier types. Dedoped PEDOT:PSS has a reduced dark carrier density, which enhances its selectivity by facilitating efficient hole transport while blocking electrons. This improved selectivity leads to a notable increase in the R_{sh}, thus reducing unwanted shunt currents. Consequently, the elevated R_{sh} contributes to heightened FF values, promoting overall solar cell efficiency.

Table 1. Photovoltaic parameters extracted from the J-V curve of Sn-Pb PSC employing dedoped PEDOT:PSS as HTL. The photovoltaic parameters reported are averaged from a sample of 8 devices. (The champion device is highlighted in bold)

Condition	PCE (%)	V_{OC} (V)	J_{SC} (mA/cm^2)	FF (%)
PEDOT:PSS	19.1 (±0.62)	0.85 (±0.01)	30.46(±0.59)	74.1(±1.8)
	19.7	**0.85**	**31.6**	**73.5**
Dedoping 5%	19.8 (±0.46)	0.86 (±0.01)	30.48(±0.56)	75.5(±1.6)
	20.7	**0.87**	**31.3**	**76.7**
Dedoping 10%	21.3 (±0.78)	0.88 (±0.01)	30.77(±0.77)	79.1 (±1.5)
	22.6	**0.89**	**31.6**	**80.2**
Dedoping 20%	18.6 (±1.19)	0.86(±0.02)	29.39(±0.96)	73.9(±3.6)
	20.7	**0.87**	**30.8**	**76.9**

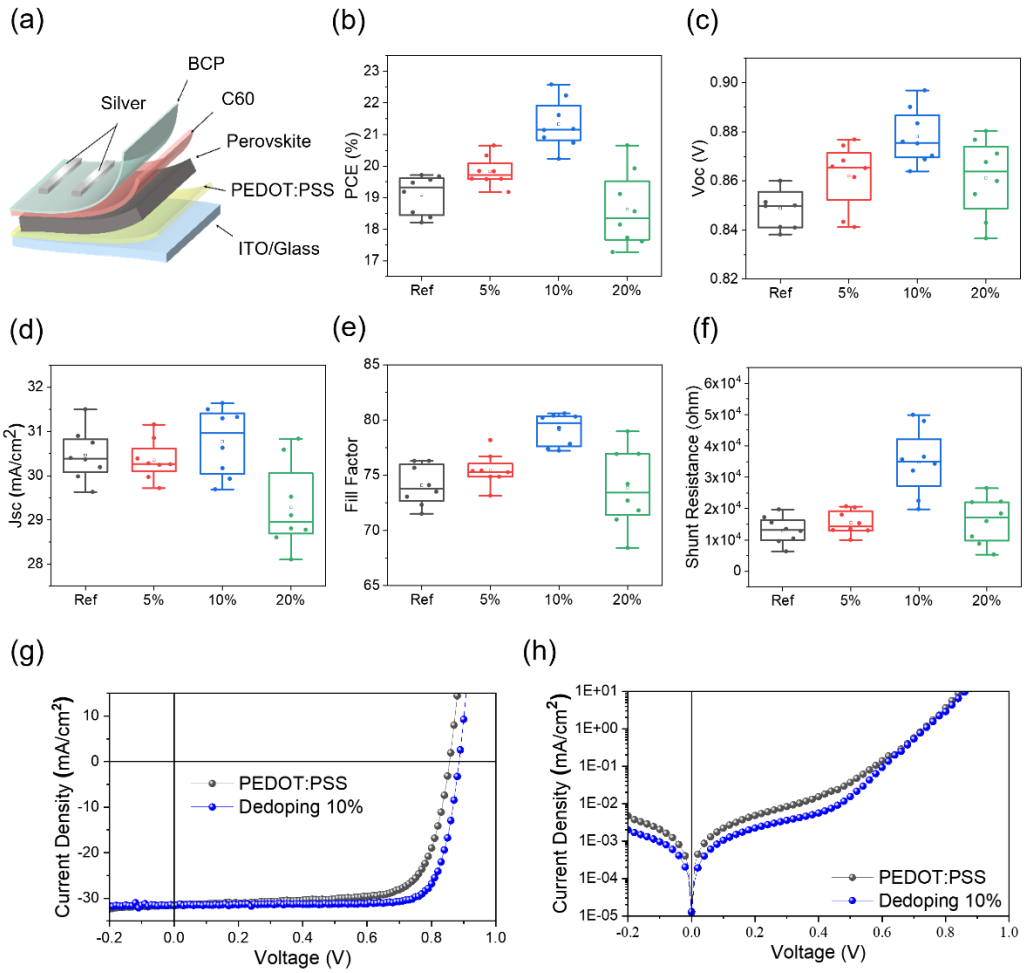

Figure 3. (a) The configuration of the device. The statistics of Photovoltaic parameters of different dedoped PEDOT:PSS devices, including (b) PCE, (c) V_{OC}, (d) J_{SC}, (e) FF, and (f)shunt resistance. The photovoltaic parameters reported are averaged from a sample of 8 devices. An independent samples t-test revealed the improved photovoltaic parameters were statistically significant ($P < 0.001$) (g) Current density-voltage curve for different dedoped PEDOT:PSS devices. (h) Dark current density-voltage curve for different dedoped PEDOT:PSS devices.

To gain deeper insight into the improved device performance, we investigated the optoelectronic properties within a structure consisting of glass/HTL/perovskite. The V_{OC} of a PSC is known to be closely linked to the PL emission of the perovskite when paired with a charge transport layer.[67–69] An increased PL emission of the perovskite in conjunction with a charge transport layer could indicate reduced recombination at the interface,[70,71] suggesting the potential for a higher V_{OC}. It has been established that the diffusion of ionic defects within the perovskite layer can limit the potential drop to a thin space charge layer near the device interfaces, keeping the perovskite bulk devoid of an electric field.[72,73] The screening effect enables electron diffusion to the HTL-

perovskite interface, potentially causing the recombination of photogenerated electrons and holes in the HTL.[52] Consequently, the doped HTL, with its high hole density, can facilitate interfacial recombination with photogenerated electrons in the perovskite layer, as depicted in **Figure 4a.** The measured PL spectra of glass/perovskite and glass/HTL/perovskite along with the corresponding changes in PL peak intensity and peak position are shown in **Figure 4b-c**. Compared with the glass/perovskite, there is 91% PL quenching when interfacing with the doped PEDOT:PSS. This observation is consistent with the previous study in Pb perovskite,[52] indicating that strong interfacial recombination occurs at this interface in Sn-Pb systems too. Importantly, when PEDOT:PSS is dedoped using NaOH, the PL intensity rises reaching a maximum for the 10 vol% NaOH dedoped sample, approximately eight times higher than the one deposited on doped PEDOT:PSS. This change of PL intensity is closely correlated with the V_{OC} increase observed for the Sn-Pb devices (**Figure 3c).** Additionally, a slight blue shift of the PL peak is observed among the samples with dedoped PEDOT:PSS layers, which can be assigned to reduced trap states in perovskite.[74]

To quantitatively evaluate recombination losses at the interface, we employed PL quantum yield (PLQY) measurements (**Figure 4d)**. PLQY is correlated with the quasi-Fermi level splitting (QFLS) throughout the device, making it a valuable predictor for the implied V_{OC}.[75,76] A higher PLQY observed in a bare perovskite film or half-cell would suggest a greater achievable V_{OC} in a fully assembled device. In the absence of PEDOT:PSS, the perovskite film exhibits a PLQY value of 6.63%. However, this value drops significantly to 0.14% when the perovskite film is placed on doped PEDOT:PSS. This decrease indicates that the interface between the perovskite film and doped PEDOT:PSS plays a critical role in reducing V_{OC} in Sn-Pb PSC. Remarkably, under the optimal conditions identified in this study, dedoping PEDOT:PSS with 10 vol% NaOH results in a substantial improvement in PLQY, increasing it from 0.14% to 0.68%. This increase in PLQY correlates well with the enhancement of device V_{OC}. Therefore, the higher magnitude of PLQY confirms an efficient suppression of recombination at the PEDOT:PSS/perovskite interface.[77]

Next, we turn our focus to time-correlated single photon counting (TCSPC) which is used to further analyze the decay kinetics, and the fitting results are shown in **Figure 4e**. The average charge carrier lifetimes, τ, for PEDOT:PSS/perovskite and dedoped PEDOT:PSS/perovskite are 250 and 629 ns, respectively. While analyzing such transient behaviors can be complicated, a more extended monomolecular lifetime at low illumination intensity suggests diminished non-radiative decay, either inside the bulk perovskite material, which is supported by enlarged grain observed in SEM images, or at the junctions between perovskite and PEDOT:PSS. This further confirms that the

dedoping of PEDOT:PSS contributes to reduced non-radiative recombination, which is beneficial for overall device performance.

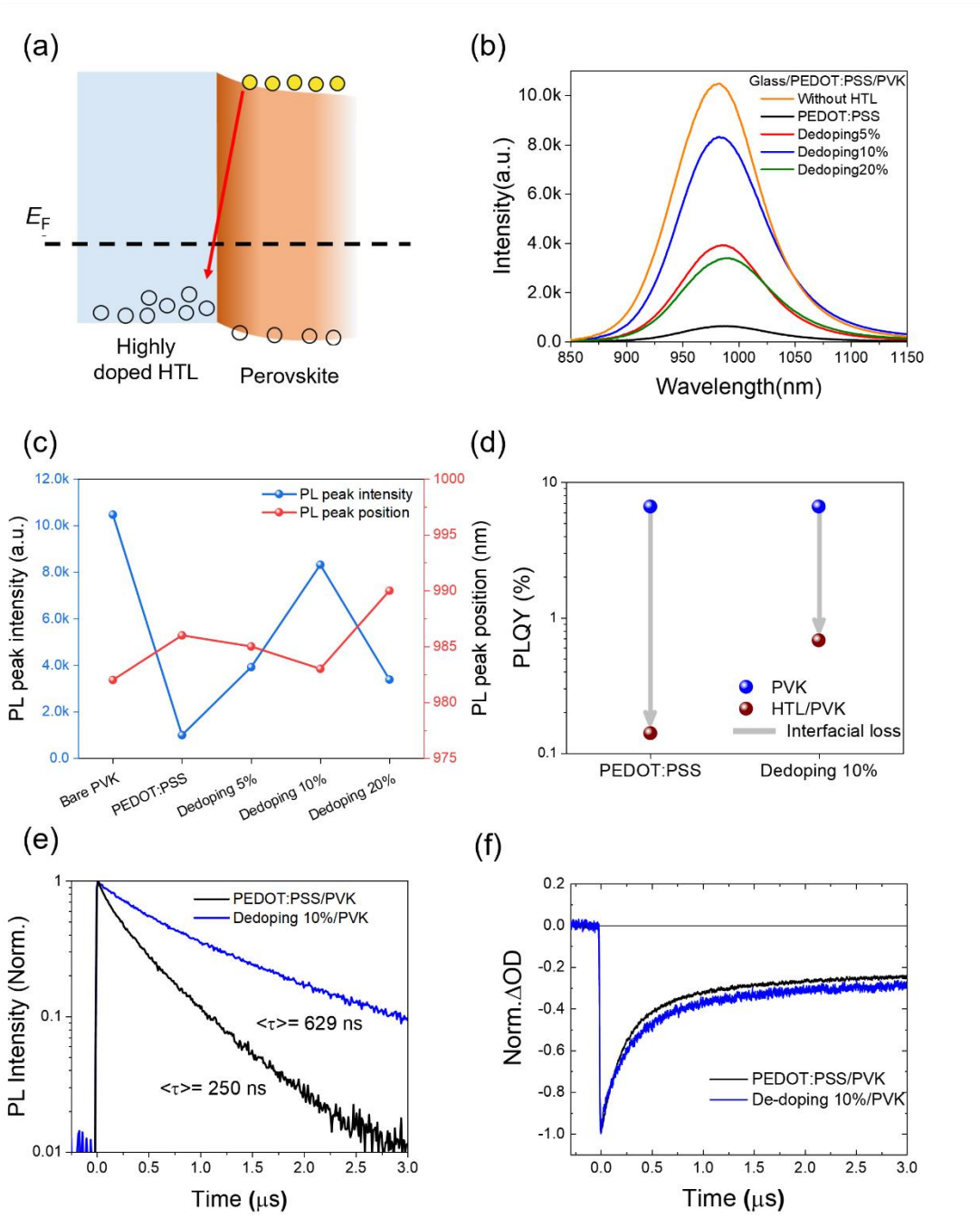

Figure 4. (a) An illustration figure of surface recombination at Sn-Pb perovskite/PEDOT:PSS interface. (b) Photoluminescence spectra of PEDOT:PSS/ Sn-Pb perovskite bilayer with varying vol% of NaOH, and (c) corresponding PL peak intensity and peak position. (d)PLQY results for Sn-Pb perovskite, PEDOT:PSS/Sn-Pb perovskite, and dedoped PEDOT:PSS/Sn-Pb perovskite. The dedoped PEDOT:PSS is with 10vol% NaOH. (e) TCSPC spectroscopy of perovskite on PEDOT:PSS and dedoped PEDOT:PSS. (f) Kinetics of GSB (ground-state

bleaching) recovery of transient absorption spectra (TAS) evolution within 3μs at 550 nm for perovskite on reference PEDOT:PSS and dedoped PEDOT:PSS.

To further understand the role of dedoping PEDOT:PSS layers in solar cell devices, we employed ns-TAS to investigate the charge carrier dynamics. Due to the moisture-sensitive nature of Sn-Pb perovskite, all films were encapsulated within a nitrogen-filled glovebox, employing a structure of glass/perovskite, glass/PEDOT:PSS/perovskite, and glass/dedoped PEDOT:PSS/perovskite, respectively. Before conducting ns-TAS measurements, UV-visible absorption spectroscopy was performed for all experimental conditions, which revealed no significant change in absorption as shown in the UV-Visible absorption spectrum (**Figure S5**). The ns-TAS results, depicted in **Figure S6a-c**, exhibited a prominent feature among all films: a negative change in optical density (ΔOD) with a peak centered at 550 nm, corresponding to ground state bleaching (GSB). To explore the decay kinetics of GSB within a 3 μs range for all experimental conditions, the ns-TAS spectra were presented in **Figure 4f** and fitted using a biexponential function. The fitting results are summarized in **Table S2**, where τ_1 and τ_2 represent the bimolecular recombination and the recombination of free carriers in the radiative channel, respectively.[78–80] Comparing the faster decay component, τ_1, it is observed that the perovskite film on PEDOT:PSS (192 ns) exhibits a shorter value than that on dedoped PEDOT:PSS layer (203 ns). This difference indicates faster bimolecular recombination occurring at the interface between PEDOT:PSS and perovskite. As the recombination rate is proportional to the number of electrons and holes,[7,81] the faster bimolecular recombination process in the PEDOT:PSS/perovskite bilayer can be attributed to the higher density of holes in PEDOT:PSS. The GSB is associated with the electron population in the valance band. Therefore, comparing the slower decay component τ_2, it can observed that PEDOT:PSS/perovskite and dedoped PEDOT:PSS/perovskite exhibit values of 983 ns and 873 ns, respectively. The larger τ_2 in the PEDOT:PSS/perovskite bilayer suggests relatively unchanged ΔOD at longer time scales (>1 μs), indicating that the majority of electrons recombine to the ground state within shorter time scales. On the other hand, the smaller τ_2 in dedoped PEDOT:PSS/perovskite indicates that a portion of electrons recombines to the ground state at longer time scales. Surface photovoltage (SPV) measurements further confirm the faster rate of recombination in the case of the PEDOT:PSS sample compared to the dedoped one (**Figure S7**). The positive sign of SPV means an increased density of electrons at the surface of the perovskite under illumination in both cases, however when the light is turned off a large spike appears for the PEDOT:PSS/perovskite sample, which is not present if the PEDOT:PSS is dedoped. The generated SPV signal is a quasi-equilibrium product of the photogeneration of charge carriers, their recombination, and

charge transport. The presence and disappearance of a spike in SPV is the result of the rate of charge recombination changing with respect to the charge transport rate. This suggests that there is faster bimolecular recombination in the PEDOT:PSS/perovskite sample under illumination, in agreement with the ns-TAS measurements. These ns-TAS and SPV results also correlate well with the TCSPC data, reflecting the prolonged lifetime in dedoped PEDOT:PSS/perovskite and implying a reduction in non-radiative recombination. **Figure S8** shows transient photocurrent (TPC) measurements for devices incorporating both reference and dedoped PEDOT:PSS layers. The findings reveal that the control device has a TPC decay time of 0.64μs, whereas the device using dedoped PEDOT:PSS shows a reduced TPC decay of 0.25μs. This observed reduction in TPC decay time with dedoped PEDOT:PSS underscores a markedly enhanced charge extraction efficiency relative to the control device.

Finally, we shift our focus to the stability of dedoped Sn-Pb PSCs. The acidity of PEDOT:PSS is proven to cause interface instability in various devices, including organic light-emitting diodes (OLEDs),[57] organic photovoltaics (OPVs),[82] and PSCs.[83] Thus, dedoping PEDOT:PSS with NaOH, a strong base, is anticipated to alter its acidic nature to basic. **Figure S9** demonstrates that the pH value of PEDOT:PSS shifts from ~2 to ~11, indicating its transition to a basic nature upon dedoping. To characterize their interface stability, devices with pristine and dedoped PEDOT:PSS were stored in a nitrogen-filled glovebox, and their J-V characteristics were measured periodically. **Figure 5** and **Table S3** reveals that the device using pristine PEDOT:PSS experiences a ~37% PCE reduction, declining from 18.5% to 11.7% after 1176 hours, primarily due to FF degradation stemming from increased series resistance. Conversely, the device featuring dedoped PEDOT:PSS displays only a ~7% PCE reduction, dropping from 22.6% to 21.1%. It has been demonstrated that the acidity of PEDOT:PSS can cause corrosion of ITO, subsequently leading to the diffusion of indium into both the PEDOT:PSS and the active layer in organic and perovskite devices.[83–85] Such corrosion and indium contamination can be mitigated by alkalizing the PEDOT:PSS,[83] which is likely a major factor in improving the lifetime of the Sn-Pb PSCs with dedoped PEDOT:PSS in this study.

We further explore the stability under other environmental stress. **Figure S10** highlights the stability of devices stored in the air, revealing that both devices undergo accelerated degradation compared to those preserved in an N_2 atmosphere. This is likely due to oxidation, particularly the conversion of Sn^{2+} to Sn^{4+}, which plays a significant role in the observed degradation of both the reference and dedoped devices.[33] **Figure S11** presents the results of light stability assessments carried out under 1 sun illumination at open-circuit conditions, showing that devices with dedoped

PEDOT:PSS have improved longevity compared to the reference cells. At last, thermal stability tests were performed at 85°C for both reference and dedoped devices, as shown in **Figure S12**. We observed that the thermal stability of our devices significantly depends on the electrode selection. This suggests that factors other than the Sn-Pb perovskite layer, such as electrodes or transport layers, might be limiting the thermal stability. This observation is in agreement with existing literature.[65,86–88] In summary, while dedoped PEDOT:PSS enhances the stability of Sn-Pb perovskite under specific conditions, such as in nitrogen or under illumination, a thorough investigation into the overall stability of the complete Sn-Pb device, including both the transport layer and electrodes, merits further exploration.

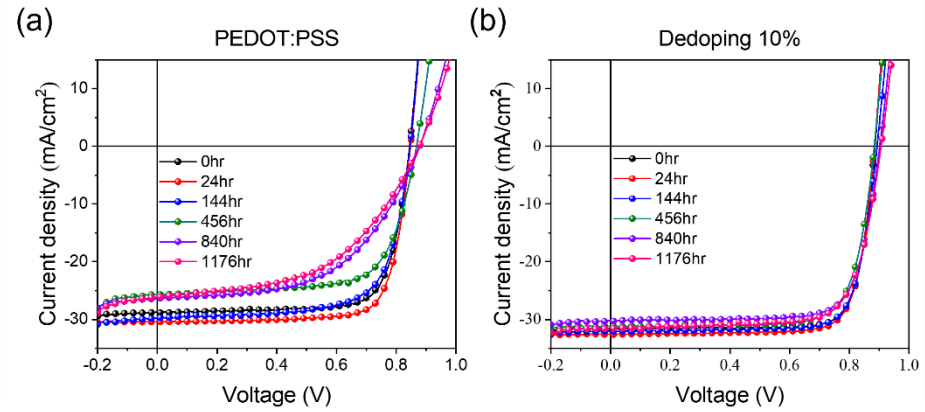

Figure 5. The current density-voltage curve of Sn-Pb PSC employing (a) PEDOT:PSS and (b) dedoped PEDOT:PSS with 10 vol% NaOH as HTL. The devices were stored in N_2 filled glovebox and measured periodically under 1 sun solar simulator.

Conclusion

In conclusion, our study reveals that PEDOT:PSS, commonly employed as a hole transport layer in Sn-Pb perovskite devices, leads to surface recombination and limited open-circuit voltage due to its highly doped nature. We demonstrate that NaOH serves as an effective dual-functional dedoping agent. It reduces the hole population within PEDOT:PSS by deprotonating sulfonated groups, which leads to a decrease in work function and conductivity. Additionally, sodium ions from dedoped PEDOT:PSS improve the crystallinity of the Sn-Pb perovskite film, enhancing grain size and ultimately device performance. By reducing the dark carrier density, dedoping enhances the selectivity of the hole transport layer, increasing shunt resistance and boosting the fill factor in Sn-Pb perovskite solar cells. Consequently, our approach offers straightforward means to significantly improve power conversion efficiencies in mixed Sn-Pb perovskite solar cells, elevating device performance from 19.7% to 22.6%. Moreover, dedoping PEDOT:PSS with NaOH significantly improves device stability, reducing power conversion efficiency loss from approximately 37% to under 7% after 1176 h in an N_2 atmosphere. This work underscores the importance of dedoping strategies to mitigate interfacial recombination losses in Sn-Pb perovskite solar cells. These findings also offer valuable insights for the design of single-junction perovskite solar cells as well as all-perovskite tandem solar cells.

Supporting Information

Supporting Information is available from the author.

Conflicts of interest

There are no conflicts to declare.

Acknowledgments

C.-T. L. thanks to the National Science and Technology Council (110-2222-E-005-005 -MY3, 112-2628-E-005 -002 -), and Innovation and Development Center of Sustainable Agriculture from The Featured Areas Research Center Program within the framework of the Higher Education Sprout Project by the Ministry of Education (MOE) in Taiwan. T.J.M. thanks the Royal Commission for the Exhibition of 1851 for their financial support through a Research Fellowship. T.J.M also acknowledges funding from a Royal Society University Research Fellowship (URF/R1/221834) and the Royal Society

Research Fellows Enhanced Research Expenses (RF/ERE/221066). M.D. and S.E. acknowledge the funding of UK Engineering and Physical Sciences Research Council (EPSRC) provided via grant EP/S030727/1. Additionally, thanks are given for the SIMS measurement assistance from the Instrumentation Center at National Tsing Hua University. H.C. acknowledges financial support from the National Research Foundation of Korea (NRF) grant funded by the Korea government (MSIT) (RS-2023-00213920).

Reference

[1] J. Y. Kim, J. W. Lee, H. S. Jung, H. Shin, N. G. Park, *Chem Rev* **2020**, *120*, 7867.

[2] B. Chen, P. N. Rudd, S. Yang, Y. Yuan, J. Huang, *Chem Soc Rev* **2019**, *48*, 3842.

[3] J. Park, J. Kim, H. S. Yun, M. J. Paik, E. Noh, H. J. Mun, M. G. Kim, T. J. Shin, S. Il Seok, *Nature* **2023**, *616*, 724.

[4] Q. Jiang, J. Tong, Y. Xian, R. A. Kerner, S. P. Dunfield, C. Xiao, R. A. Scheidt, D. Kuciauskas, X. Wang, M. P. Hautzinger, R. Tirawat, M. C. Beard, D. P. Fenning, J. J. Berry, B. W. Larson, Y. Yan, K. Zhu, *Nature* **2022**, *611*, 278.

[5] X. Yang, D. Luo, Y. Xiang, L. Zhao, M. Anaya, Y. Shen, J. Wu, W. Yang, Y. H. Chiang, Y. Tu, R. Su, Q. Hu, H. Yu, G. Shao, W. Huang, T. P. Russell, Q. Gong, S. D. Stranks, W. Zhang, R. Zhu, *Advanced Materials* **2021**, *33*, 1.

[6] H. Zhou, Q. Chen, G. Li, S. Luo, T. Song, H.-S. Duan, Z. Hong, J. You, Y. Liu, Y. Yang, *Science (1979)* **2014**, *345*, 542.

[7] T. S. Sherkar, C. Momblona, L. Gil-Escrig, J. Ávila, M. Sessolo, H. J. Bolink, L. J. A. Koster, *ACS Energy Lett* **2017**, *2*, 1214.

[8] T. J. Macdonald, A. J. Clancy, W. Xu, Z. Jiang, C. Lin, L. Mohan, T. Du, D. D. Tune, L. Lanzetta, G. Min, T. Webb, A. Ashoka, R. Pandya, V. Tileli, M. A. Mclachlan, J. R. Durrant, S. A. Haque, C. A. Howard, *J Am Chem Soc* **2021**, *143*, 21549.

[9] N. J. Jeon, J. H. Noh, W. S. Yang, Y. C. Kim, S. Ryu, J. Seo, S. Il Seok, *Nature* **2015**, *517*, 476.

[10] K. A. Bush, K. Frohna, R. Prasanna, R. E. Beal, T. Leijtens, S. A. Swifter, M. D. McGehee, *ACS Energy Lett* **2018**, *3*, 428.

[11] D. Chi, S. Huang, M. Zhang, S. Mu, Y. Zhao, Y. Chen, J. You, *Adv Funct Mater* **2018**, *28*, 1804603.

[12] C. T. Lin, F. De Rossi, J. Kim, J. Baker, J. Ngiam, B. Xu, S. Pont, N. Aristidou, S. A. Haque, T. Watson, M. A. McLachlan, J. R. Durrant, *J Mater Chem A Mater* **2019**, *7*, 3006.

[13] F. Gao, Y. Zhao, X. Zhang, J. You, *Adv Energy Mater* **2019**, 1902650.

[14] X. Zheng, B. Chen, J. Dai, Y. Fang, Y. Bai, Y. Lin, H. Wei, X. C. Zeng, J. Huang, *Nat Energy* **2017**, *2*, 17102.

[15] T. Du, S. R. Ratnasingham, F. U. Kosasih, T. J. Macdonald, L. Mohan, A. Augurio, H. Ahli, C. T. Lin, S. Xu, W. Xu, R. Binions, C. Ducati, J. R. Durrant, J. Briscoe, M. A. McLachlan, *Adv Energy Mater* **2021**, *11*, 2101420.

[16] T. Du, T. J. Macdonald, R. X. Yang, M. Li, Z. Jiang, L. Mohan, W. Xu, Z. Su, X. Gao, R. Whiteley, C. Lin, G. Min, S. A. Haque, J. R. Durrant, K. A. Persson,

M. A. Mclachlan, J. Briscoe, *Advanced Materials* **2022**, *34*, 2107850.

[17] Z. Xiao, Q. Dong, C. Bi, Y. Shao, Y. Yuan, J. Huang, *Advanced Materials* **2014**, *26*, 6503.

[18] Y. Zhou, Z. Wang, J. Jin, X. Zhang, J. Zou, F. Yao, Z. Zhu, X. Cui, D. Zhang, Y. Yu, C. Chen, D. Zhao, Q. Cao, Q. Lin, Q. Tai, *Angewandte Chemie - International Edition* **2023**, *62*, e202300759.

[19] A. Magomedov, A. Al-Ashouri, E. Kasparavičius, S. Strazdaite, G. Niaura, M. Jošt, T. Malinauskas, S. Albrecht, V. Getautis, *Adv Energy Mater* **2018**, *8*, 1801892.

[20] C. M. Wolff, L. Canil, C. Rehermann, N. L. Nguyen, F. Zu, M. Ralaiarisoa, P. Caprioglio, L. Fiedler, M. Stolterfoht, S. Kogikoski Jr, I. Bald, N. Koch, E. L. Unger, T. Dittrich, A. Abate, D. Neher, *ACS Nano* **2020**, *14*, 1445.

[21] F. M. Rombach, S. A. Haque, T. J. Macdonald, *Energy Environ Sci* **2021**, *14*, 5161.

[22] X. Zhou, L. Zhang, X. Wang, C. Liu, S. Chen, M. Zhang, X. Li, W. Yi, B. Xu, *Advanced Materials* **2020**, *32*, 1908107.

[23] S. Gu, R. Lin, Q. Han, Y. Gao, H. Tan, J. Zhu, *Advanced Materials* **2020**, *32*, 1907392.

[24] A. Goyal, S. McKechnie, D. Pashov, W. Tumas, M. Van Schilfgaarde, V. Stevanović, *Chemistry of Materials* **2018**, *30*, 3920.

[25] J. Wen, Y. Zhao, Z. Liu, H. Gao, R. Lin, S. Wan, C. Ji, K. Xiao, Y. Gao, Y. Tian, J. Xie, C. J. Brabec, H. Tan, *Advanced Materials* **2022**, *34*, 2110356.

[26] J. Tong, Z. Song, D. Hoe Kim, X. Chen, C. Chen, A. F. Palmstrom, P. F. Ndione, M. O. Reese, S. P. Dunfield, O. G. Reid, J. Liu, F. Zhang, S. P. Harvey, Z. Li, S. T. Christensen, G. Teeter, D. Zhao, M. M. Al-Jassim, M. F. A M van Hest, M. C. Beard, S. E. Shaheen, J. J. Berry, Y. Yan, K. Zhu, *Science (1979)* **2019**, *364*, 475.

[27] J. Tong, Q. Jiang, A. J. Ferguson, A. F. Palmstrom, X. Wang, J. Hao, S. P. Dunfield, A. E. Louks, S. P. Harvey, C. Li, H. Lu, R. M. France, S. A. Johnson, F. Zhang, M. Yang, J. F. Geisz, M. D. McGehee, M. C. Beard, Y. Yan, D. Kuciauskas, J. J. Berry, K. Zhu, *Nat Energy* **2022**, *7*, 642.

[28] R. Lin, Y. Wang, Q. Lu, B. Tang, J. Li, H. Gao, Y. Gao, H. Li, C. Ding, J. Wen, P. Wu, C. Liu, S. Zhao, K. Xiao, Z. Liu, C. Ma, Y. Deng, L. Li, F. Fan, H. Tan, *Nature* **2023**, *620*, 994.

[29] J. Wang, M. A. Uddin, B. Chen, X. Ying, Z. Ni, Y. Zhou, M. Li, M. Wang, Z. Yu, J. Huang, *Adv Energy Mater* **2023**, *13*, 2204115.

[30] R. Lin, Y. Wang, Q. Lu, B. Tang, J. Li, H. Gao, Y. Gao, H. Li, C. Ding, J. Wen, P. Wu, C. Liu, S. Zhao, K. Xiao, Z. Liu, C. Ma, Y. Deng, L. Li, F. Fan, H. Tan,

Nature **2023**, *620*, 994.

[31] M. A. Green, E. D. Dunlop, M. Yoshita, N. Kopidakis, K. Bothe, G. Siefer, X. Hao, *Progress in Photovoltaics: Research and Applications* **2023**, *31*, 651.

[32] K. Xiao, R. Lin, Q. Han, Y. Hou, Z. Qin, H. T. Nguyen, J. Wen, M. Wei, V. Yeddu, M. I. Saidaminov, Y. Gao, X. Luo, Y. Wang, H. Gao, C. Zhang, J. Xu, J. Zhu, E. H. Sargent, H. Tan, *Nat Energy* **2020**, *5*, 870.

[33] T. Leijtens, R. Prasanna, A. Gold-Parker, M. F. Toney, M. D. McGehee, *ACS Energy Lett* **2017**, *2*, 2159.

[34] L. Lanzetta, T. Webb, N. Zibouche, X. Liang, D. Ding, G. Min, R. J. E. Westbrook, B. Gaggio, T. J. Macdonald, M. S. Islam, S. A. Haque, *Nat Commun* **2021**, *12*, 2853.

[35] Q. Liu, A. Li, W. Chu, O. V. Prezhdo, W. Z. Liang, *J Mater Chem A Mater* **2022**, *10*, 234.

[36] J. W. Lee, S. H. Bae, N. De Marco, Y. T. Hsieh, Z. Dai, Y. Yang, *Mater Today Energy* **2018**, *7*, 149.

[37] Y. Ma, H. Zhang, Y. Zhang, R. Hu, M. Jiang, R. Zhang, H. Lv, J. Tian, L. Chu, J. Zhang, Q. Xue, H. L. Yip, R. Xia, X. Li, W. Huang, *ACS Appl Mater Interfaces* **2019**, *11*, 3044.

[38] C. Li, Z. Song, D. Zhao, C. Xiao, B. Subedi, N. Shrestha, M. M. Junda, C. Wang, C.-S. Jiang, M. Al-Jassim, R. J. Ellingson, N. J. Podraza, K. Zhu, Y. Yan, *Adv Energy Mater* **2019**, *9*, 1803135.

[39] Z. Zhang, J. Liang, Y. Zheng, X. Wu, J. Wang, Y. Huang, Y. Yang, Z. Zhou, L. Wang, L. Kong, K. M. Reddy, C. Qin, C. C. Chen, *J Mater Chem A Mater* **2021**, *9*, 17830.

[40] S. Hu, K. Otsuka, R. Murdey, T. Nakamura, M. A. Truong, T. Yamada, T. Handa, K. Matsuda, K. Nakano, A. Sato, K. Marumoto, K. Tajima, Y. Kanemitsu, A. Wakamiya, *Energy Environ Sci* **2022**, *15*, 2096.

[41] H. Liu, L. Wang, R. Li, B. Shi, P. Wang, Y. Zhao, X. Zhang, *ACS Energy Lett* **2021**, *6*, 2907.

[42] T. J. Macdonald, L. Lanzetta, X. Liang, D. Ding, S. A. Haque, *Advanced Materials* **2023**, *35*, 2206684.

[43] L. Lanzetta, T. Webb, J. M. Marin-Beloqui, T. J. Macdonald, S. A. Haque, *Angewandte Chemie - International Edition* **2023**, *62*, e202213.

[44] J. P. Correa Baena, L. Steier, W. Tress, M. Saliba, S. Neutzner, T. Matsui, F. Giordano, T. J. Jacobsson, A. R. Srimath Kandada, S. M. Zakeeruddin, A. Petrozza, A. Abate, M. K. Nazeeruddin, M. Grätzel, A. Hagfeldt, *Energy Environ Sci* **2015**, *8*, 2928.

[45] L. Gil-Escrig, C. Momblona, M. Sessolo, H. J. Bolink, *J Mater Chem A Mater*

2016, *4*, 3667.

[46] H. Hu, S. Moghadamzadeh, R. Azmi, Y. Li, M. Kaiser, J. C. Fischer, Q. Jin, J. Maibach, I. M. Hossain, U. W. Paetzold, B. Abdollahi Nejand, *Adv Funct Mater* **2022**, *32*, 2107650.

[47] G. Kapil, T. Bessho, Y. Sanehira, S. R. Sahamir, M. Chen, A. K. Baranwal, D. Liu, Y. Sono, D. Hirotani, D. Nomura, K. Nishimura, M. A. Kamarudin, Q. Shen, H. Segawa, S. Hayase, *ACS Energy Lett* **2022**, *7*, 966.

[48] Z. Yu, J. Wang, B. Chen, M. A. Uddin, Z. Ni, G. Yang, J. Huang, *Advanced Materials* **2022**, *34*, 2205769.

[49] P. Guo, J. Dong, C. Xu, Y. Yao, J. You, H. Bian, W. Zeng, G. Zhou, X. He, M. Wang, X. Zhou, M. Wang, Q. Song, *J Mater Chem A Mater* **2023**, *11*, 7246.

[50] M. Zhang, D. Chi, J. Wang, F. Wu, S. Huang, *Solar Energy* **2020**, *201*, 589.

[51] M. Daboczi, I. Hamilton, S. Xu, J. Luke, S. Limbu, J. Lee, M. A. McLachlan, K. Lee, J. R. Durrant, I. D. Baikie, J. S. Kim, *ACS Appl Mater Interfaces* **2019**, *11*, 46808.

[52] T. Du, W. Xu, M. Daboczi, J. Kim, S. Xu, C.-T. Lin, H. Kang, K. Lee, M. J. Heeney, J.-S. Kim, J. R. Durrant, M. A. McLachlan, *J Mater Chem A Mater* **2019**, *7*, 18971.

[53] Y. C. Chin, M. Daboczi, C. Henderson, J. Luke, J. S. Kim, *ACS Energy Lett* **2022**, *7*, 560.

[54] J. Wu, H. Cha, T. Du, Y. Dong, W. Xu, C. T. Lin, J. R. Durrant, *Advanced Materials* **2022**, *34*, 2101833.

[55] J. Werner, T. Moot, T. A. Gossett, I. E. Gould, A. F. Palmstrom, E. J. Wolf, C. C. Boyd, M. F. A. M. Van Hest, J. M. Luther, J. J. Berry, M. D. McGehee, *ACS Energy Lett* **2020**, *5*, 1215.

[56] T. C. Tsai, H. C. Chang, C. H. Chen, Y. C. Huang, W. T. Whang, *Org Electron* **2014**, *15*, 641.

[57] M. M. De Kok, M. Buechel, S. I. E. Vulto, P. Van De Weyer, E. A. Meulenkamp, S. H. P. M. De Winter, A. J. G. Mank, H. J. M. Vorstenbosch, C. H. L. Weijtens, V. Van Elsbergen, *Physica Status Solidi A Appl Res* **2004**, *201*, 1342.

[58] T. P. A. Van Der Pol, S. T. Keene, B. W. H. Saes, S. C. J. Meskers, A. Salleo, Y. Van De Burgt, R. A. J. Janssen, *Journal of Physical Chemistry C* **2019**, *123*, 24328.

[59] H. Cho, W. Cho, Y. Kim, J. G. Lee, J. H. Kim, *RSC Adv* **2018**, *8*, 29044.

[60] T. Sedghamiz, A. Y. Mehandzhiyski, M. Modarresi, M. Linares, I. Zozoulenko, *Chemistry of Materials* **2023**, *35*, 5512.

[61] J. Huang, P. F. Miller, J. S. Wilson, A. J. De Mello, J. C. De Mello, D. D. C.

Bradley, *Adv Funct Mater* **2005**, *15*, 290.
[62] D. Alemu, H. Y. Wei, K. C. Ho, C. W. Chu, *Energy Environ Sci* **2012**, *5*, 9662.
[63] S. Bag, M. F. Durstock, *ACS Appl Mater Interfaces* **2016**, *8*, 5053.
[64] Y. He, J. Wang, R. Tang, D. Yao, S. Li, P. Dong, C. Li, F. Long, *J Alloys Compd* **2023**, *933*, 167583.
[65] C. T. Lin, J. Ngiam, B. Xu, Y. H. Chang, T. Du, T. J. Macdonald, J. R. Durrant, M. A. McLachlan, *J Mater Chem A Mater* **2020**, *8*, 8684.
[66] C. Bi, Q. Wang, Y. Shao, Y. Yuan, Z. Xiao, J. Huang, *Nat Commun* **2015**, *6*, 7747.
[67] J. Kim, R. Godin, S. D. Dimitrov, T. Du, D. Bryant, M. A. McLachlan, J. R. Durrant, *Adv Energy Mater* **2018**, *8*, 1802474.
[68] M. Stolterfoht, V. M. Le Corre, M. Feuerstein, P. Caprioglio, L. J. A. Koster, D. Neher, *ACS Energy Lett* **2019**, *4*, 2887.
[69] C.-T. Lin, W. Xu, T. J. Macdonald, J. Ngiam, J.-H. Kim, T. Du, S. Xu, P. S. Tuladhar, H. Kang, K. Lee, J. R. Durrant, M. A. McLachlan, *ACS Appl Mater Interfaces* **2021**, *13*, 43505.
[70] W. Xu, L. J. F. Hart, B. Moss, P. Caprioglio, T. J. Macdonald, F. Furlan, J. Panidi, R. D. J. Oliver, R. A. Pacalaj, M. Heeney, N. Gasparini, H. J. Snaith, P. R. F. Barnes, J. R. Durrant, *Adv Energy Mater* **2023**, *13*, 2301102.
[71] M. Stolterfoht, P. Caprioglio, C. M. Wolff, J. A. Márquez, J. Nordmann, S. Zhang, D. Rothhardt, U. Hörmann, Y. Amir, A. Redinger, L. Kegelmann, F. Zu, S. Albrecht, N. Koch, T. Kirchartz, M. Saliba, T. Unold, D. Neher, *Energy Environ Sci* **2019**, *12*, 2778.
[72] R. A. Belisle, W. H. Nguyen, A. R. Bowring, P. Calado, X. Li, S. J. C. Irvine, M. D. McGehee, P. R. F. Barnes, B. C. O'Regan, *Energy Environ Sci* **2017**, *10*, 192.
[73] P. Calado, A. M. Telford, D. Bryant, X. Li, J. Nelson, B. C. O'Regan, P. R. F. Barnes, *Nat Commun* **2016**, *7*, 13831.
[74] Y. Shao, Z. Xiao, C. Bi, Y. Yuan, J. Huang, *Nat Commun* **2014**, *5*, 6784.
[75] M. Stolterfoht, P. Caprioglio, C. M. Wolff, J. A. Márquez, J. Nordmann, S. Zhang, D. Rothhardt, U. Hörmann, Y. Amir, A. Redinger, L. Kegelmann, F. Zu, S. Albrecht, N. Koch, T. Kirchartz, M. Saliba, T. Unold, D. Neher, *Energy Environ Sci* **2019**, *12*, 2778.
[76] P. Caprioglio, M. Stolterfoht, C. M. Wolff, T. Unold, B. Rech, S. Albrecht, D. Neher, *Adv Energy Mater* **2019**, *9*, 1901631.
[77] S. Hu, P. Zhao, K. Nakano, R. D. J. Oliver, J. Pascual, J. A. Smith, T. Yamada, M. A. Truong, R. Murdey, N. Shioya, T. Hasegawa, M. Ehara, M. B. Johnston, K. Tajima, Y. Kanemitsu, H. J. Snaith, A. Wakamiya, *Advanced Materials*

2023, *35*, 2208320.

[78] G. Xing, N. Mathews, S. Sun, S. S. Lim, Y. M. Lam, M. Graẗzel, S. Mhaisalkar, T. C. Sum, *Science (1979)* **2013**, *342*, 344.

[79] S. D. Stranks, G. E. Eperon, G. Grancini, C. Menelaou, M. J. P. Alcocer, T. Leijtens, L. M. Herz, A. Petrozza, H. J. Snaith, S. D. Stranks, G. E. Eperon, G. Grancini, C. Menelaou, M. J. P. Alcocer, T. Leijtens, L. M. Herz, A. Petrozza, H. J. Snaith, *Science (1979)* **2013**, *342*, 341.

[80] Y. Yang, W. Rodríguez-Córdoba, T. Lian, *J Am Chem Soc* **2011**, *133*, 9246.

[81] D. Głowienka, D. Zhang, F. Di Giacomo, M. Najafi, S. Veenstra, J. Szmytkowski, Y. Galagan, *Nano Energy* **2020**, *67*, 104186.

[82] H. Kim, S. Nam, H. Lee, S. Woo, C. S. Ha, M. Ree, Y. Kim, *Journal of Physical Chemistry C* **2011**, *115*, 13502.

[83] Q. Wang, C. C. Chueh, M. Eslamian, A. K. Y. Jen, *ACS Appl Mater Interfaces* **2016**, *8*, 32068.

[84] Y. Meng, Z. Hu, N. Ai, Z. Jiang, J. Wang, J. Peng, Y. Cao, *ACS Appl Mater Interfaces* **2014**, *6*, 5122.

[85] M. Jørgensen, K. Norrman, F. C. Krebs, *Solar Energy Materials and Solar Cells* **2008**, *92*, 686.

[86] Y. Kato, L. K. Ono, M. V. Lee, S. Wang, S. R. Raga, Y. Qi, *Adv Mater Interfaces* **2015**, *2*, 1500195.

[87] J. Zhao, X. Zheng, Y. Deng, T. Li, Y. Shao, A. Gruverman, J. Shield, J. Huang, *Energy Environ Sci* **2016**, *9*, 3650.

[88] C.-T. Lin, S. Pont, J. Kim, T. Du, S. Xu, X. Li, D. Bryant, M. A. Mclachlan, J. R. Durrant, *Sustain Energy Fuels* **2018**, *2*, 1686.